

Investigation on Deformation Behavior of Nickel Aluminum Bronze by Neutron Diffraction and Transmission Electron Microscopy



XIAOYAN XU, HONG WANG, YUTING LV, WEIJIE LU, and GUANGAI SUN

The deformation behavior, deformation microstructures, and generated inter-phase stresses of nickel aluminum bronze were investigated by *in situ* neutron diffraction instrument and transmission electron microscopy in this paper. Lattice strains calculated by both peak shifting and broadening by Gaussian fitting of α and κ phase neutron diffraction peak profiles at both holding stress conditions and unloaded stress conditions were compared. Twinning and stacking faults in α matrix were observed after deformed by different tensile stresses. Compressive internal/residual stress in α matrix and tensile internal stress in κ phase in elasto-plastic region were calculated based on neutron diffraction analysis. The piled-up dislocations around hard κ phases increase with increasing the deformation degree, which raise the stress concentration near α/κ interface and increase the internal stresses.

DOI: 10.1007/s11661-016-3379-9

© The Minerals, Metals & Materials Society and ASM International 2016

I. INTRODUCTION

NICKEL aluminum bronze (NAB) alloys are widely used for marine components due to their good combination of strength, fracture toughness, and corrosion resistance.^[1–4] Cast NAB consists of coarse α grain, four kinds of iron- and nickel-rich intermetallic phases, and island martensite β' phase.^[5–8] Microstructures, mechanical properties, and corrosion behaviors of as-cast NAB have already been investigated in many papers.^[3,9,10] It was reported that κ phases with different morphologies and chemical compositions from different heat treatments led to the changes of mechanical properties and corrosion properties.^[5]

The investigation of twinning faults and stacking faults in deformed pure copper has reported that twinning tendency is higher in material with a lower stacking fault energy in face-centered cubic (FCC) metals.^[11–13] For Cu-Al alloy, increasing Al concentration reduces the stacking fault energy, also the twin thickness.^[14] Strength of materials increases with increasing twin boundary density especially in polycrystalline copper.^[15] Transmission electron microscopy (TEM) is utilized to capture the direct deformation structures, but it is difficult to quantitatively analyze the microstructure

parameters under tensile deformation.^[16] Therefore, neutron diffraction technology which has a deep penetration capability into most metallic materials and a unique volume-averaged bulk measurement ability becomes a promising method to investigate the deformation behavior of metals.^[17,18] Jeong *et al.*^[19] obtained the microstructure parameters of austenitic steel including probabilities of twin/stacking fault formations, stacking fault energy, and dislocation density by analyzing peak position, breadth, and asymmetry of peak diffraction profiles. In addition, neutron diffraction technique can also be used to detect the accumulation of internal/residual intergranular stresses on multiphase alloys due to its phase-selective feature.^[20] Deformation at certain range on multiphase alloy (such as NAB) would generate significant internal stresses due to the heterogeneous mechanical properties. The inter-phase type intergranular stress between different phases and intergranular stress between various crystal orientations but in the same phase both belong to the internal stress (Type II microstrain). By employing neutron diffraction instrument, Wilson *et al.*^[21] found that the internal stress in ferrite matrix was balanced by that in carbide particles. Similar phenomenon was also observed by Bonner *et al.*^[22] in a pearlitic high-carbon steel that there is a high axial elastic tensile strain developed in cementite phase in compensation of a reduced strain in ferrite. Todd *et al.*^[23] measured the residual microstrains of Alumina matrix and SiC particles in composite when temperature changed by neutron diffraction and depicted how inter-phase stresses favor the fracture mode transition. Different from the soft copper solid solution matrix, the intermetallic alloys Fe₃Al and NiAl have a hard and brittle nature.^[24–26] Therefore, the inter-phase stress (Type II microstrain) between α matrix and κ phases might be generated when NAB is deformed in the elasto-plastic regime. However, there is little

XIAOYAN XU, Research Associate, YUTING LV, Ph.D. Candidate, and WEIJIE LU, Fellow Researcher, are with the State Key Laboratory of Metal Matrix Composites, Shanghai Jiao Tong University, No. 800 Dongchuan Road, Materials Science and Engineering Building D329, Minhang District, Shanghai 200240, P.R. China. Contact e-mail: luweijie@sjtu.edu.cn HONG WANG, Senior Engineer, and GUANGAI SUN, Associate Professor, are with the Key Laboratory of Neutron Physics and Institute of Nuclear Physics and Chemistry, China Academy of Engineering Physics, Mianyang 621999, P.R. China.

Manuscript submitted August 29, 2015.

Article published online February 17, 2016

published research related to the deformation behavior of NAB alloy including the inter-phase stress formation, not to mention the measurement of this stress.

In this paper, neutron diffraction instrument and TEM were used to characterize the deformation behavior including α matrix and κ phases, make observation of stacking faults and twin faults, and estimate the dislocation density by two methods after the tensile deformation. This paper will help identify the role of second phases on deformation behavior of NAB multiphase alloy, provide detailed deformation microstructures by TEM observation, and illuminate the correlation of inter-phase stress and dislocation density around second phases.

II. EXPERIMENTAL PROCEDURE

A. Material

The NAB cast ingot with a dimension of ϕ 150 mm \times 200 mm was prepared by vacuum melting. Chemical composition of the as-cast NAB was determined by fluorescence spectrophotometer as 9.85 wt pct Al, 3.86 wt pct Fe, 3.76 wt pct Ni, 1.03 wt pct Mn, and balance Cu. Samples used in this paper were cut from the ingot center to diminish the heterogeneous microstructure, then annealed in furnace at 948 K (675 °C) for 2 hours in order to decrease the volume fraction of retained β phase and relief the residual stress.

B. In Situ Neutron Diffraction Experiment

The *in situ* neutron diffraction experiments were conducted by Residual Stress Neutron Diffraction Instrument (RSND) at China Academy of Engineering Physics in Mianyang. Test sample was wire-electrode sectioned to a dog bone shape with a gage length of 40 mm, width of 4 mm, and thickness of 4 mm. The sample was fixed in the stress rig and then loaded along the longitudinal direction (gage length). The crystal planes parallel to the loading direction in the test sample were measured by diffraction test. A strain extensometer with 10 mm gage length was used to record the instantaneous strain of the test sample during the *in situ* tensile test. Neutron diffraction measurements were conducted with the diffraction angle of $2\theta = 44, 45.5, \text{ and } 51.5$ deg, which corresponded to the reflections of Cu (111), Fe_3Al (200)/NiAl (110), and Cu (200), respectively, by a constant wavelength of $\lambda = 0.1587$ nm. By setting the incident slit and diffracted slit as 4×4 mm², a diamond-shaped gage volume was obtained. In order to avoid the shift of the diffracted gage volume centroid during the tensile procedure, the bidirectional tensile loading function of the stress rig is used during the *in situ* test.^[27] Therefore, the reflection plane peak position is not shifting during the deformation. The detailed specifications of RSND diffractometer and the stress rig are listed in Reference 27 with a 0.1 mm accuracy of tensile direction positioning. The stress-free condition and seven loading stress conditions (200, 300, 400, 450, 500, 550, and 600 MPa) were chosen to conduct

the neutron diffraction test to obtain the deformation behaviors at different static loading stresses. Also, six unloaded conditions (load released from 300, 400, 450, 500, 550, and 600 MPa) were chosen to conduct the diffraction test for obtaining the residual strain of each phase. When the load applies to all phases in NAB in the elastic region then unloaded, the strain formed within all the phases by elastic deformation will disappear. When the applied load increases into elasto-plastic region, plastic deformation occurs in preferred grains (α grains), but not in the hard grains (κ phases). The elastic strain developed in phases to accommodate inhomogeneous plastic deformation is the inter-phase strain, which will become type II residual strain (microstrain) after the load is removed.^[28] So by using this tensile load-unload test, the internal strains we measured by neutron diffraction become type II microstrain without type I residual strain (macrostrains). The diffraction times for Cu (111), Fe_3Al (200)/NiAl(110), and Cu (200) diffraction profiles are set as 5, 15, and 8 minutes in order to collect the similar intensities of each peak, respectively. Gaussian fitting was used to analyze the peak profiles as suggested by ISO/TS 21432: 2005 international standard method (Non-destructive testing: Standard test method for determining of residual stresses by neutron diffraction).

C. Mechanical Properties and Microstructure Observation

Annealed NAB material was wire-electrode cut to dog bone-shaped tensile bars, ground with SiC abrasive paper on the sample surface, and pulled by ZwickT1 test machine with a strain rate of 10^{-3} s⁻¹. Three bars were used to obtain the tensile mechanical properties, and others were tensile loaded to certain stress and unloaded, then prepared for TEM observation. The annealed NAB sample was cold mounted, grounded, polished, and then etched by a solution of 5 g $\text{FeCl}_3 + 2$ mL HCl + 95 mL $\text{C}_2\text{H}_5\text{OH}$ at room temperature. Optical microscopy was used to observe the morphology of different phases. Volume fraction of each phase was analyzed by Image-Pro Plus software based on the optical images. The phase structure is also identified by a D8 ADVANCE X-ray diffractometer with Cu K_α radiation at room temperature. The deformed NAB samples were sectioned to thin plates, mechanical polished to 100 μm thickness, then twin-jet electro-polished using a solution of 33 pct $\text{HNO}_3 + 67$ pct CH_3OH at -25 °C. JEM-200 EX transmission electron microscope was used to characterize the deformation behavior of these NAB samples.

III. RESULTS

A. Annealed NAB Microstructure

The microstructure of annealed NAB sample is shown in Figure 1(a) which contains α grains as matrix, retained β phase (β' phase), and three kinds of nickel-iron-aluminum intermetallic phases (κ_{II} , κ_{III} ,

and κ_{IV} indicated by light arrows in Figure 1(a). Image-Pro Plus was employed to estimate the volume fraction of each phase. Phase κ_{II} appears to have a globular dendritic structure which has a volume fraction of 10 pct. Phase κ_{III} appears to have a lamellar eutectoid microstructure and coexists with α lamellae and has a volume fraction of 7 pct. Fine κ_{IV} precipitate well distributes within α grains and has a volume fraction of 5 pct. The martensitic retained β phase displays the darkest contrast in Figure 1(a) with only 1 pct volume fraction. The retained β phase could transform to κ_{III} lamellar structure when annealed at 948 K (675 °C).^[6]

The X-ray diffraction pattern of the annealed NAB is shown in Figure 1(b). The rough estimation of κ phase volume fraction in NAB samples is about 15 pct from intensity ratio of Cu (111) and NiAl (110)/Fe₃Al (220) peak obtained by the X-ray diffraction test.

B. Peak Shifting and Broadening

Two peaks of copper solid solution and one peak of κ phase were employed to monitor the neutron diffraction profiles at tensile deformation process. Figure 2 shows the diffraction profiles at 2θ of around 51, 44, and 45.5 deg when NAB was holding at different tensile stresses. The solid curves in Figure 2 are Gaussian fittings for different diffraction profiles. The profiles at diffraction 2θ angles of 51 and 44 deg represent Cu (200) peak and Cu (111) peak, respectively (Figures 2(a) and (b)). It is obvious that with increasing the applied stress, the peak position shifts to lower angle and the peak breadth increases.

The profiles at 2θ of around 45.5 deg (Figure 2(c)) present both the intermetallic alloy Fe₃Al and NiAl. Phase κ_{II} in NAB is based on Fe₃Al with a DO3 structure and a lattice parameter of $5.71 \pm 0.06 \text{ \AA}$.^[5] Fine κ_{IV} particles have the similar composition and crystal structure with κ_{II} phase and with a lattice

parameter of $5.77 \pm 0.06 \text{ \AA}$. Tang *et al.*^[29] report that the strongest intensity peak of DO3 structure Fe₃Al (220) is around 45 deg. Phase κ_{III} has a B2 structure based on NiAl with a lattice parameter of $2.88 \pm 0.03 \text{ \AA}$, which also has the strongest intensity peak at around 45 deg.^[30] Also, considering that NiAl's lattice parameter has a half relationship with Fe₃Al's, the diffraction profile at 2θ of 45.5 deg is suggested to be the superposition of NiAl (110) and Fe₃Al (220) peaks. Scattering from other peaks of intermetallic NiAl and Fe₃Al phases was too weak to allow a reasonable single peak fitting. Hence, the peak profile at 45.5 deg is designated as (Fe, Ni)Al (110) on behalf of all the observed κ phases in NAB alloy. (Fe, Ni)Al (110) diffraction peak shifts to lower angle and broadens along with the stress increment, which has the similar trend with Cu (200) and Cu (111) peaks.

Figure 3 shows the diffraction profiles of Cu (200), Cu (111), and (Fe, Ni)Al (110) peaks at different unloaded conditions. Cu (200) peak shifts to higher angle but then goes back to lower angle with increasing the tensile deformation stress in Figure 3(a). Cu (111) peak shifts to higher angle in Figure 3(b), while (Fe, Ni)Al (110) peak shifts to lower angle in Figure 3(c). All three diffraction profiles broaden along with the increase of the tensile stress.

As to neutron diffraction patterns holding at different stresses, the peak position of Cu (200) shifts from 2θ of 51.37 to 50.85 deg, Cu (111) peak shifts from 44.03 to 43.90 deg, and (Fe, Ni)Al (110) peak shifts from 45.49 to 45.07 deg when the applied stress reaches 600 MPa in Figure 2. Compared with the holding stress conditions, the unloaded stress conditions in Figure 3 show a much less peak position shifting but a close peak broadening. The peak position of Cu (200) shifts from 2θ of 51.37 to 51.39 deg and then 51.31 deg, Cu (111) peak shifts from 44.03 to 44.06 deg, and (Fe, Ni)Al (110) peak shifts from 45.49 to 45.35 deg when stress unloaded from 600 MPa.

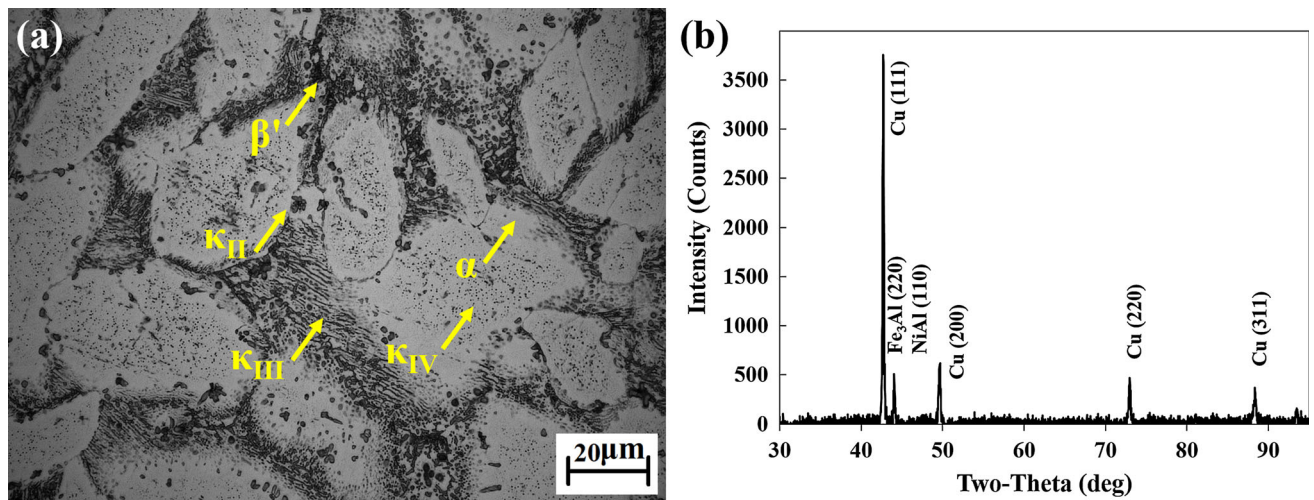


Fig. 1—(a) Microstructure of annealed NAB alloy; (b) X-ray diffraction of annealed NAB.

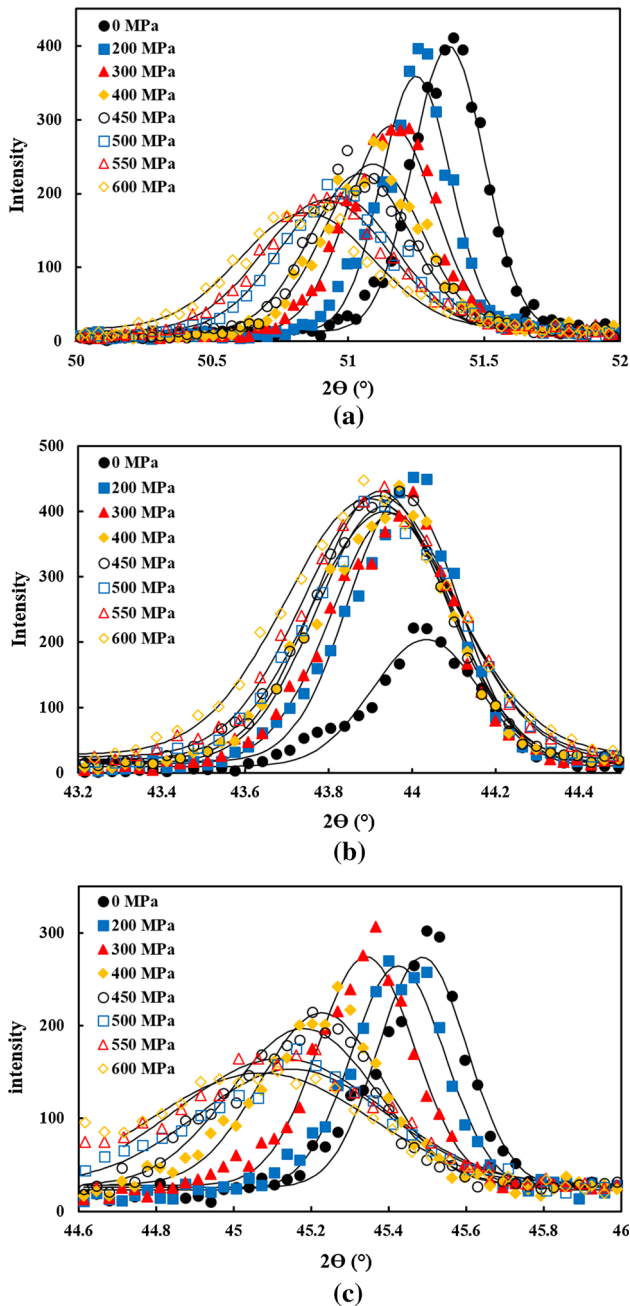


Fig. 2—Peak profiles of NAB alloy held at different stresses: (a) profiles at different 2θ angles around 51 deg representing Cu (200) peak; (b) the profiles at different 2θ angles around 44 deg representing Cu (111) peak; and (c) the profiles at different 2θ angles around 45 deg representing (Fe, Ni)Al (110) peak. The solid curves are Gaussian fitting curves from different diffraction peaks.

IV. DISCUSSION

A. Peak Full Width at Half Maximum and Lattice Strain

The lattice strains in materials can be obtained by the precise diffraction measurements on the deviation of lattice plane spacing (d_{hkl}) of particularly oriented hkl crystal planes due to the effect of stress.^[18] The lattice

strain for hkl plane can be calculated from the difference of d_{hkl} and d_{hkl}^0 (stress-free lattice spacing) measured as the center of corresponding diffraction peak at diffraction angle θ_{hkl} and θ_{hkl}^0 according to Eq. [1]:

$$\Delta\varepsilon_{hkl} = \frac{d_{hkl} - d_{hkl}^0}{d_{hkl}^0} = -\cot(\theta_{hkl})\Delta\theta_{hkl}. \quad [1]$$

The lattice strains from reflections Cu (200), Cu (111), and (Fe, Ni)Al (110) are calculated by Eq. [1]. Figure 4(a) shows the lattice strains obtained from peak shifting method with samples held at different stresses. The error of peak center position obtained by Gaussian fitting ranges from 0.005 pct (0.003 deg) to 0.03 pct (0.014 deg) for various diffraction profiles in Figure 2.

The annealed NAB sample provides 139 ± 24 GPa Young's modulus and 270 ± 30 MPa yield strength. Cu-7 pctAl contains similar Al content with α matrix of NAB which shows 115 to 131 GPa Young's modulus^[31,32] and 250 MPa yield strength.^[31] So the yield point of α phase has a high possibility to fall in the range of 200 to 300 MPa. Fe₃Al and NiAl alloys have a higher yield strength than copper, which are from 333 to 760 MPa^[33] and 400 MPa, respectively.^[26] Therefore, the region from 0 to 200 MPa is supposed to be the elastic region for both α and κ phases, which is designated as Region I in Figure 4(a). The moduli of Cu at $\langle 100 \rangle$ crystal orientation is 129, 141 GPa for Cu at $\langle 111 \rangle$ crystal orientation,^[34] 131 GPa for Fe₃Al at $\langle 110 \rangle$ crystal orientation,^[35] and 290 GPa for NiAl at $\langle 110 \rangle$ crystal orientation.^[36] The slope value of Cu (200) lattice strain–tensile stress curve in elastic region in Figure 4(a) is higher than the other two, which agrees with the lower moduli value reported above.

The lattice strain–tensile stress curves of Cu (111) and (Fe, Ni)Al (110) start to separate after 200 MPa. The main reason of the partition is that the increasing internal stress leads to the onset of plastic flow of α matrix.^[18] Cu (111) lattice strain displays a straight increment along with tensile stress from 200 to 450 MPa, then a plateau after 450 MPa. The slope of lattice strain–tensile stress curve of (Fe, Ni)Al (110) decreases slightly which could indicate a yield phenomenon of κ phase after 450 MPa. Based on the changes of lattice strain increment, Region II presents elasto-plastic regime and Region III presents equally plastic flow regime which are indicated in Figure 4. The specific reflection lattice strain is determined by the corresponding grains. Copper has a rather high elastic anisotropy, which would lead to a redistribution of load between the reflections of different oriented grains.^[37] The lattice strain redistribution between Cu (200) and Cu (111) reflections determined by a combination of elastic and plastic anisotropy is shown in Figure 4(a). From the lattice strain–tensile stress response, $\langle 111 \rangle$ orientation shows a higher diffraction elastic constants (reciprocal of slope) which indicates a stiffer character than $\langle 200 \rangle$ orientation. So, $\langle 200 \rangle$ oriented grains are softer than $\langle 111 \rangle$ in the plastic region. This phenomenon also agrees with the results of pure copper grains.^[37] It should also be noticed that the different profile

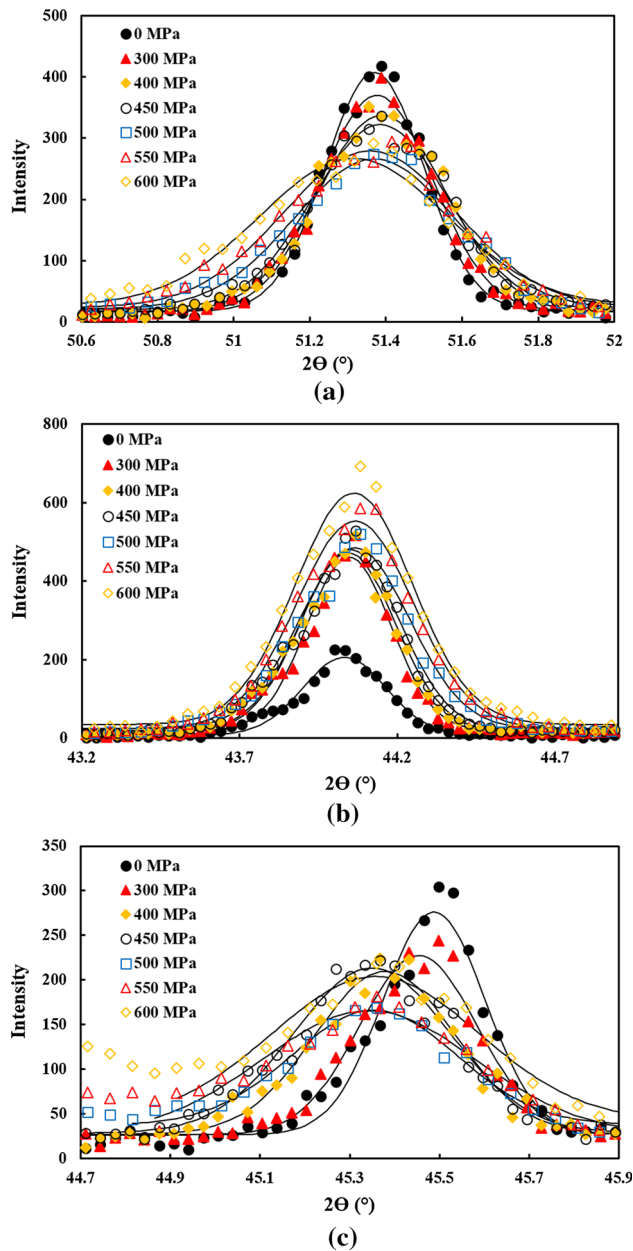


Fig. 3—Diffraction profiles at different unloaded stress conditions: (a) the profiles at different 2θ angles around 51 deg representing Cu (200) peak; (b) the profiles at different 2θ angles around 44 deg representing Cu (111) peak; and (c) the profiles at different 2θ angles around 45 deg representing (Fe, Ni)Al (110) peak. The solid curves are Gaussian fitting curves from different peak profiles.

asymmetry of the plastically deformed material could affect the accuracy of the Gaussian fitting.^[18] This suggests that the calculated lattice strain could be slightly away from the expected value due to the misfit.

Lattice strain could be obtained from both single peak position shifting and peak broadening. The values of full width at half maximum (FWHM) of diffraction profiles of Cu (200), Cu (111), and (Fe, Ni)Al (110) are shown in Figure 4(b) for samples under different stresses. The error of FWHMs obtained from Gaussian fitting is from 1.6 pct (0.006 deg) to 4.6 pct (0.037 deg) for various diffraction profiles in Figure 2. The peak profiles of Cu

(200) and Cu (111) show little broadening at elastic regime (Region I). At Region II, FWHM of copper solid solution starts to increase slowly, suggesting a yield phenomenon of α matrix. Peak broadening of κ phases takes place slowly at elastic region until 300 MPa, then the FWHM starts to increase rapidly both at Region II and Region III.

The peak broadening includes instrumental effect and physical effect. To obtain a physical contribution to the broadening, the line profile of the standard sample (annealed stress-free sample) is determined first. After refining the physically broadened profile parameters, the main lattice strain can be calculated by the difference of microstrain from FWHM^[38]:

$$\Delta\epsilon_{hkl} = \frac{\beta_{hkl} - \beta_{hkl}^0}{4 \tan(\theta_{hkl})}, \quad [2]$$

where β_{hkl} is the FWHM for hkl crystal plane after deformation and β_{hkl}^0 is the FWHM for stress-free condition. Lattice strains of α and κ phases calculated from Eq. [2] are plotted in Figure 4(c). Compared with the lattice strain calculated from peak shifting method in Figure 4(a), FWHM approach provides less information for plastic behavior with smaller lattice strain values. On the other hand, lattice strain can influence the peak broadening in turn. Besides the lattice strain, subgrains generated by plastic deformation may also lead to the variation of FWHM values. What is more, the formation of stacking faults and twin faults makes contribution to change the peak profile shape such as inducing peak profile asymmetry as well.^[19] All these reasons bring about an inaccuracy of calculated FWHM values and result in a difference of the two estimated lattice strains from approaches (Eqs. [1] and [2]).

B. Twin and Stacking Faults

Figure 5(a) shows the microstructure of twins generated after 300 MPa tensile deformation. Figure 5(b) sketches a domain which clearly presents two neighbors with a symmetric and coherent structure with each other. Figure 5(c) shows the twins formed after 500 MPa tensile deformation, with a distinct symmetric structure observed by HRTEM in Figure 5(d). What is more, the diffraction pattern shown in the inset of Figure 5(d) indicates a twin microstructure from the domain in Figure 5(c) which is same as the pure copper twin pattern.^[39]

Twinning is more frequently observed in FCC materials with a relatively low stacking fault energy.^[13] For Cu-Al alloy, stacking fault energy has a proportional relationship with the twin thickness. The average value of twin thickness decreases monotonically with increasing Al concentration at the range of 1 pct to 4.5 pct.^[14] The average twin thickness of copper solid solution in α matrix is from 43 to 65 nm deformed from 300 to 600 MPa by TEM observation of NAB alloy. These values are close to the twin thickness of Cu-Al alloy at room temperature.^[14] Considering the same strain rate and temperature used in the NAB tensile test, different observation areas with various element contents

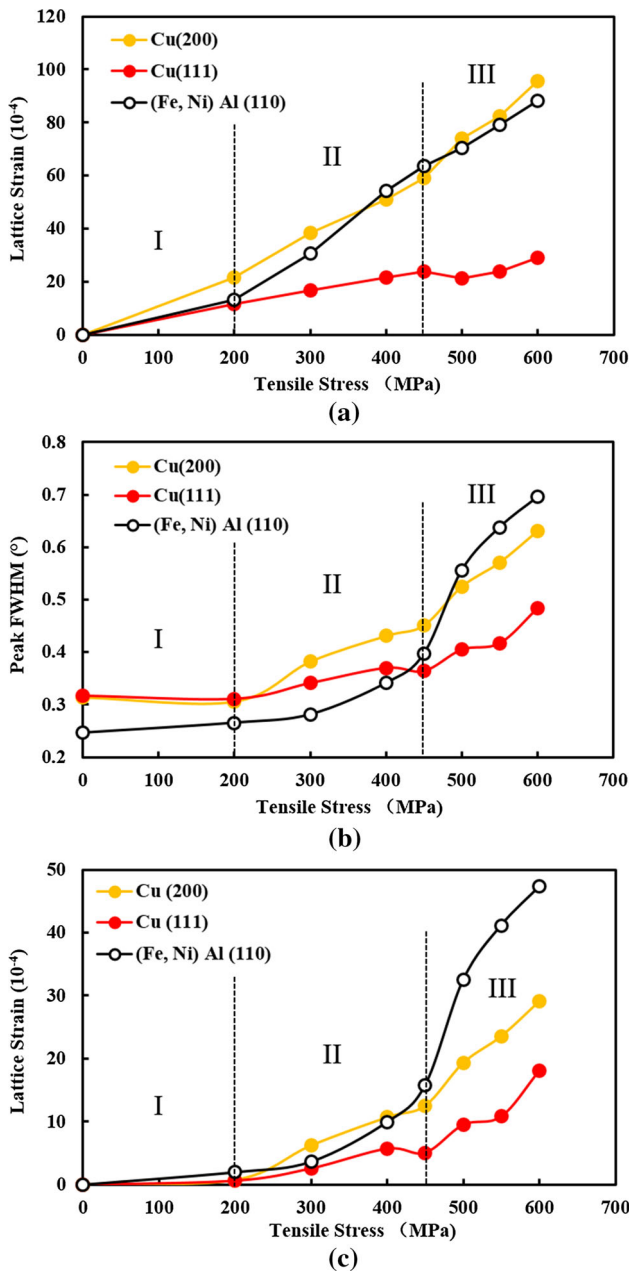


Fig. 4—(a) Lattice strains obtained from peak position shifting vs different holding stresses; (b) FWHMs of diffraction profiles vs different holding stresses; and (c) lattice strains calculated based on FWHM vs different holding stresses.

(including Al, Mn, Cr, Fe, and Ni) would be one of the main reasons for the variation of the twin thickness.

Twin-fault probability is directly related with the peak asymmetry,^[40] and this value can be calculated directly from the peak profile and the split function parameters.^[41] The twin-fault probability has a proportional tendency with the tensile strain, but it is also affected by the amount of alloying elements.^[19] In Figure 2(a), the Cu (200) peak profile at stress-free condition shows the best peak symmetry with a Gaussian fitting R^2 equal to 99.1 pct, compared with 98.2 pct for 500 MPa and 97.5 pct for 600 MPa. The Cu (200) peak profile of

deformed sample exhibits a slight peak asymmetry that some points are away from the fitted Gaussian profiles in the half-peak position. However, it is not obvious that the number of twin faults is significantly increased with increasing the tensile stress under the observation of TEM.

The chemical composition of the square shape particles in Figure 6(a) is 15.6 pct Al, 2.5 pct Cr, 2.3 pct Mn, 47.3 pct Fe, 1.8 pct Ni, and 30.6 pct Cu in atomic percent. The 3:1 atomic ratio of Fe to Al indicates that the observed particle is κ_{IV} phase. The morphology of this kind of κ_{IV} particle is also reported by Hasan *et al.*^[42] Stacking faults are first observed around κ_{IV} particles and interact with them after 300 MPa tensile deformation in Figure 6(a). The stacking faults seem to appear first at the particle convex which has a high stress concentration and then propagate into α matrix. After 400 MPa deformation, crossed stacking faults start to appear (90 deg between two stacking faults), and the quantity of stacking faults increases (Figure 6(b)). After 500 MPa deformation, more stacking faults and dislocations are present as shown in Figure 6(c), and the intersection angle of two stacking faults decreases to around 80 deg. After 600 MPa deformation, the quantity of stacking faults is not increased significantly, but the intersection angle reduces to around 45 deg, which might be due to the severe plastic deformation of α matrix. Jeong *et al.*^[19] report that stacking fault probability and twin-fault probability are proportional to tensile strain, which agrees with the phenomenon in Figure 6 that higher degree deformation results in higher amount of stacking faults.

C. Dislocation Density

The dislocation density of different phases at various orientations can be obtained by Williamson method expressed by Eq. [3]^[43,44]:

$$\rho_{hkl} = \frac{2\sqrt{3}}{|\vec{b}|} \cdot \frac{\langle \varepsilon_{hkl}^2 \rangle^{1/2}}{D_{hkl}}, \quad [3]$$

where ρ_{hkl} is the dislocation density of particularly oriented hkl crystal plane, ε_{hkl}^2 is the weighted average of ε_{hkl}^2 after multiple measuring, $|\vec{b}|$ represents the mold of Burger's vector, and D_{hkl} is the domain size which can be expressed by Eq. [4]^[38]:

$$D_{hkl} = \frac{\lambda}{\beta_{hkl} \cos(\theta_{hkl})}, \quad [4]$$

where λ is the wavelength of neutron which is 0.1587 nm in this paper. Burger's vector \vec{b} can be calculated by the relationship of $\vec{b} = \sqrt{2}a/2$ for copper solid solution. Dislocations obtained from peak broadening are a result of both the lattice strains caused by total dislocation content and the lattice rotations caused by accumulation of excess dislocations within dislocation walls. Excess dislocation has a proportional relationship with peak broadening, and also related with the misorientation

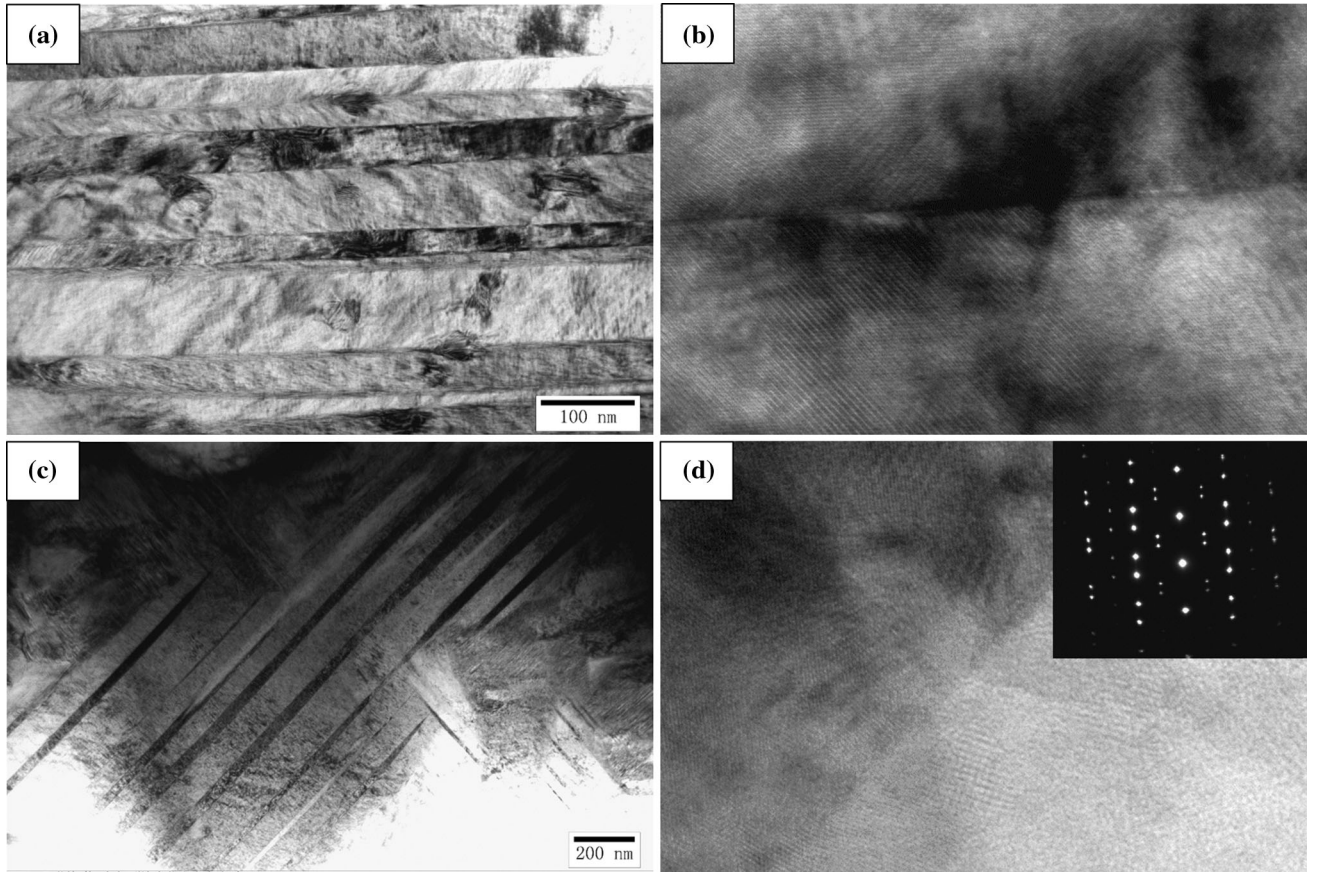


Fig. 5—(a) Twin microstructure generated after 300 MPa tensile deformation; (b) HRTEM image of twin microstructure in (a); twin microstructure generated after 500 MPa tensile deformation; (d) HRTEM image of twin microstructure in (c).

between adjacent cells.^[45] Breuer *et al.*^[45] calculated the excess dislocation at different strains (plotted in Figure 7) and indicated that they are smaller than the mean total dislocation densities determined from peak broadening of X-ray diffraction.

Taylor relationship between the flow stress and the square root of the mean total dislocation density is also employed to estimate the dislocation density in this paper^[45]:

$$\tau = \tau_0 + \alpha G \left| \vec{b} \right| (\rho_d)^{1/2}, \quad [5]$$

where τ is the shear stress, τ_0 is the friction stress which is 5 MPa for copper polycrystals, and α is the interaction constant which is around 0.245.^[45] In order to make consistent with dislocation density calculation obtained from Eq. [3], flow stress and shear moduli of Cu (111) orientation in NAB samples were chosen. The dislocation density of α matrix calculated by Eq. [5] is shown in Figure 7. The dislocation density obtained from Williamson method provides a lower value than that from Taylor method after tensile strain exceeded 0.05. When the strain is around 0.1, the two methods provide close results of dislocation density, which also agree with Breuer's estimation (also calculated based on Taylor relationship). It is reported that in the strain hardening range for copper metal, the dislocation density increases

rapidly and reaches a magnitude of 10^{14} to 10^{15} m^{-2} ,^[46] which is of the same order with the results in Figure 7.

D. Inter-phase Stress

When load is applied on NAB samples, the hard phases (κ phases) are believed to take load from plastically deformed α matrix in order to maintain the stress balance inside the alloy. Similar phenomenon was reported by Oliver *et al.*^[47] who revealed a significant load transfer from the ductile ferrite matrix to cementite phase after ferrite yielded, and this relationship can also be employed to describe the stress balance behavior in the elasto-plastic region of NAB samples based on Eq. [6]:

$$\sigma_{\text{appl}} = (1 - f)\sigma_\alpha + f\sigma_\kappa, \quad [6]$$

where f is the total volume fraction of κ phases, σ_{appl} is the applied stress, σ_α is the stress the matrix taken, and σ_κ is the stress the κ phases taken. Stresses at different crystal orientations can be roughly estimated by Hooke's law:

$$\sigma_{hkl} = E_{hkl} \times \varepsilon_{hkl}. \quad [7]$$

Volume fractions of different phases were obtained from image analysis based on Figure 1(a). Taking

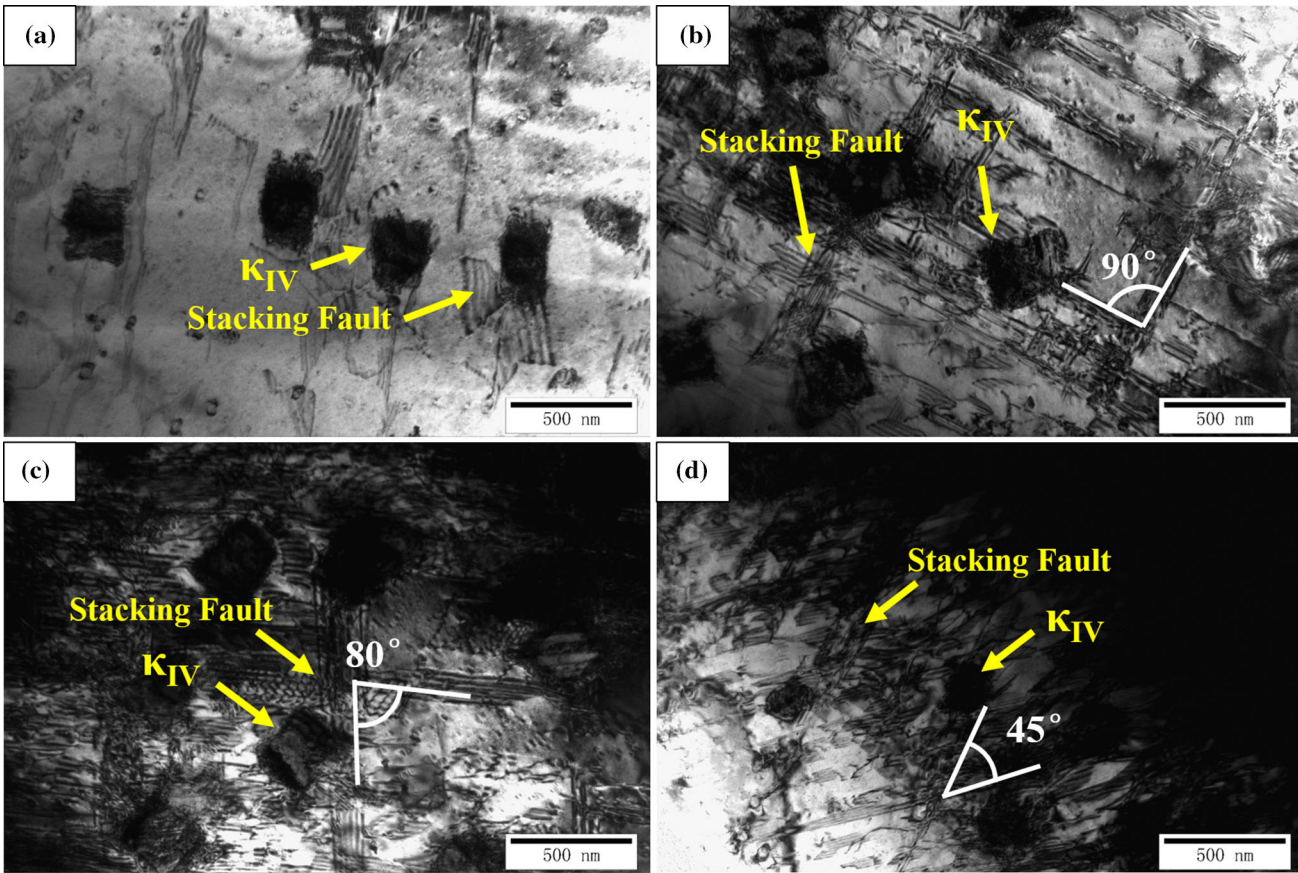


Fig. 6—Stacking faults around κ_{IV} particles after (a) 300 MPa tensile deformation; (b) 400 MPa tensile deformation; (c) 500 MPa tensile deformation; and (d) 600 MPa tensile deformation.

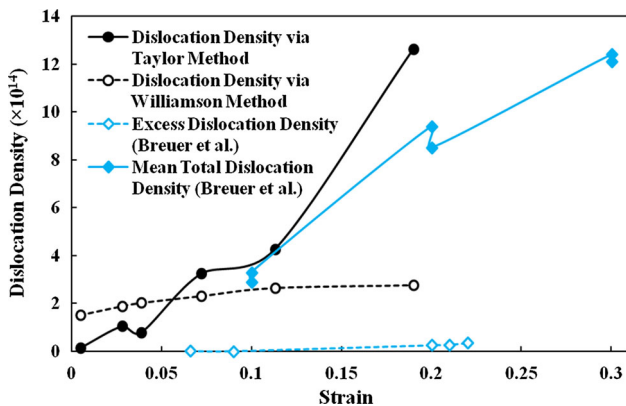


Fig. 7—Dislocation densities calculated from flow stress compared with the dislocation density from other resource.

applied tensile stress of 450 MPa and the strongest intensity peaks Cu (111) and (Fe, Ni)Al (110) for example (lattice strains used in this estimation are from Figure 4(a)), the stress sheared by α phase is estimated to be 258 MPa and the total stress sheared by κ phases (including Fe_3Al and NiAl) is about 254 MPa. The stress sum of α and κ phases sheared equals 512 MPa which is slightly higher than the applied stress. That is probably because the volume fraction of κ phases

obtained from 2D surface image analysis (22 pct) is theoretically larger than the volume fraction of bulk material. The volume fraction of κ phases from X-ray diffraction analysis (15 pct) is also smaller than that from image analysis. Therefore, the stress sheared by κ phases calculated by Eqs. [6] and [7] is reasonable.

After the applied load is removed, the sum of the two internal stresses equals zero, but the local states of stresses do not. Neutron diffraction technology can detect this internal stresses due to its phase-selective feature. Figure 8(a) shows the residual lattice strains (type II microstrains) obtained from peak shifting method (by Eq. [1]) when the NAB sample unloaded from different stresses. The error of peak center position obtained from Gaussian fitting is from 0.005 pct (0.003 deg) to 0.02 pct (0.01 deg) for various diffraction profiles in Figure 3. After the NAB samples unloaded at the elasto-plastic region, inter-phase stress will be developed between phases to accommodate inhomogeneous plastic deformation. The formation of the inter-phase stress is because the preferred plastic deformation occurs in soft grains (α grains), but hard phases (κ phases) still maintain elastic deformation during loading condition.^[28] When certain reflections were chosen to measure the corresponding peak shifts for the lattice strain calculations of these unloaded samples, the specific grains (α grains or κ phase) with specific lattice orientations are mostly representative of

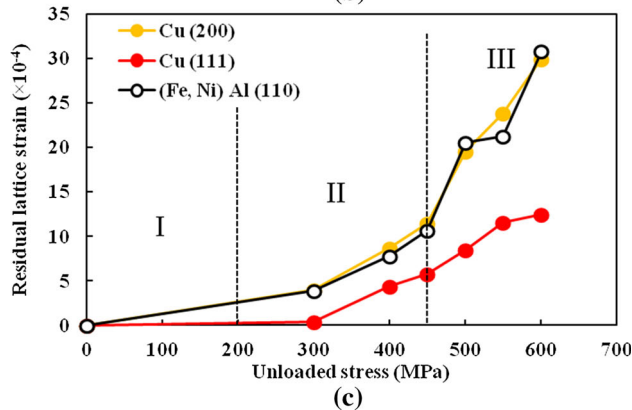
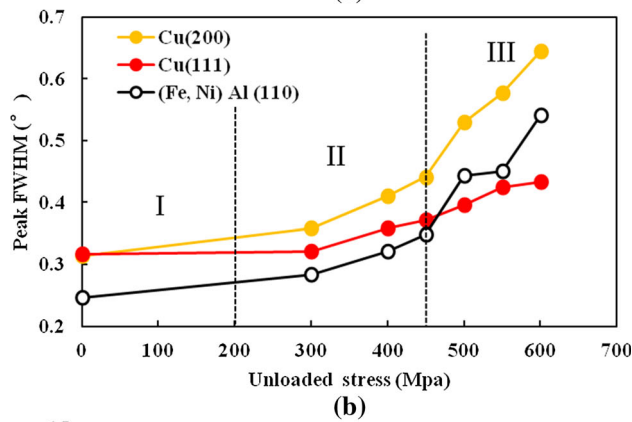
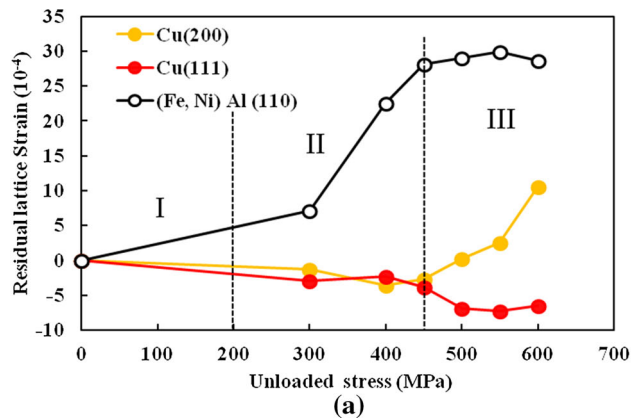


Fig. 8—(a) Lattice strains obtained from peak position shifting vs different unloaded stresses; (b) FWHMs of diffraction profiles vs different unloaded stresses; (c) lattice strains calculated based on FWHM vs different unloaded stresses.

intergranular stresses (inter-phase type intergranular stress between different phases and intergranular stress between various crystal orientations but same phase).^[48] Different from the holding stress conditions in Figure 4(a), the residual lattice strains in Figure 8(a) represent the internal strains after tensile deformation, and they are much different from each other at the three regimes. The negative residual lattice strains of reflections Cu (200) and Cu (111) at Region II represent that there is a compressive internal stress existing in α matrix, meanwhile the positive residual lattice strains of reflection (Fe, Ni)Al (110) indicate that there is an internal

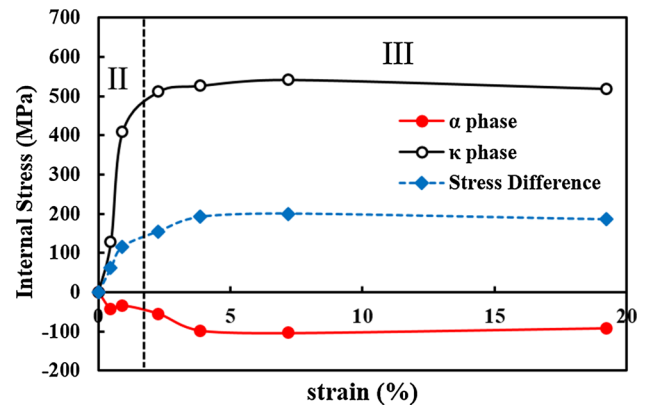


Fig. 9—Internal stresses of α matrix, κ phases, and their difference (normalized by their volume fractions) at different plastic strains.

tensile stress existing in κ phases. Also in Region II, residual lattice strain increment in α matrix stagnates with increasing the tensile stress which characterizes an elastic-to-plastic transition of copper solid solution. The significant inter-phase type intergranular stress can superimpose the intergranular stress between matrix grain families,^[20] and therefore in Region II the intergranular stress between different oriented α grains might not be observed.

Figure 9 shows the internal/residual intergranular stresses in α matrix (reflection Cu (111)), κ phases (reflection (Fe, Ni)Al (110)), and their differences (normalized by their volume fractions) at different tensile strains. At elasto-plastic Region II, the total internal stress of κ phases (inter-phase type intergranular stress) increased rapidly, raises up to 500 MPa, then remains constant, while the internal stress of α matrix only reaches up to negative 100 MPa. At Region II, the hard κ phases act as strong barriers, and the dislocations generated near phase boundaries are restricted to the original slip planer, so that the cross slip cannot occur over long-range distance. Dislocation pile-up and the stacking faults are generated near grain boundaries.^[49] The generated stacking faults near the α/κ interface boundaries can be observed in Figure 6, which increase along with the applied stress. With increasing the plastic strain in Region II, the amount of piled-up dislocations increased, and therefore the stress concentration imposed by the piled-up dislocations increases. At Region III, the internal stresses in α and κ phases stop increasing, also the difference of them, which could be related to the activation of cross slip and multiple slip.^[50] Region III reveals the fully plastic regime of both α and κ phases because the residual lattice strain of reflection (Fe, Ni)Al (110) exhibits a plateau. The large difference of residual lattice strains obtained from reflections Cu (111) and Cu (200) could be due to a significant development of intergranular stress between α grain families in Region III.

FWHM values obtained from reflections Cu (200), Cu (111), and (Fe, Ni)Al (110) are shown in Figure 8(b) for samples unloaded from different stresses. The error of FWHMs obtained from Gaussian fitting is from 1.5 pct (0.006 deg) to 4.5 pct (0.037 deg) for various peak

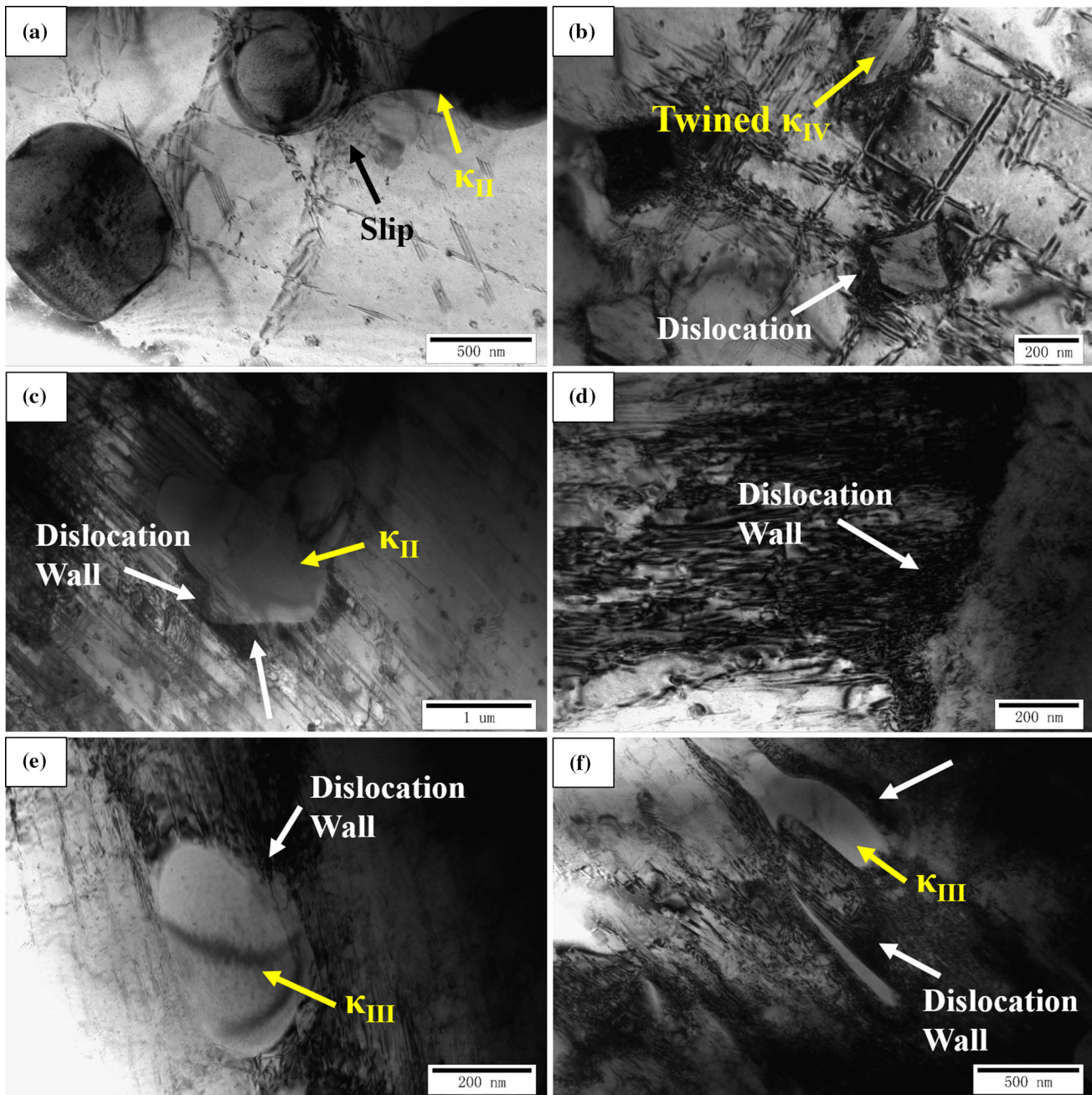


Fig. 10—Dislocation around κ phases with various shapes and compositions observed by TEM deformed with different tensile stresses: (a) 300 MPa, (b) 400 MPa, (c) and (d) 500 MPa, and (e) and (f) 600 MPa.

profiles in Figure 3. The peak breadth increases with the increase of unloaded tensile stress for both phases without apparent differences. Compared with FWHMs of holding stress condition sample profiles in Figure 4(b), FWHMs for different oriented α grains manifest close values and similar change tendency. Both FWHMs from two conditions increase from around 0.3 to 0.65 deg for Cu (200) and 0.3 to 0.45 deg for Cu (111) when tensile stress is up to 600 MPa. Defects such as dislocations, stacking faults, and twin faults are already generated when the NAB alloy was plastically deformed, and therefore the peak broadening caused by defect

accumulation could not be eliminated even if the load was removed.

Residual lattice strains of all the peak profiles were calculated based on FWHMs in Figure 8(b) by Eq. [2] and plotted in Figure 8(c). Compared with the residual lattice strain–stress response from peak position shifting method (by Eq. [1]), strains obtained from peak broadening method show no stagnating phenomenon which could be used to identify yielding phenomenon, neither positive nor negative character which could indicate tensile/compressive nature of internal stress. However, the numerical value of both kinds of residual lattice

strains would have a good agreement if the absolute values were used for comparison. This consistency suggests that both peak shifting and peak broadening are reasonable approaches to estimate the lattice strains especially for the residual strain regarding multiphase alloy.

The poor instrumental resolution of neutron diffraction results in broader diffraction peaks than those recorded by X-rays,^[49] but in this experiment all the peak broadening values of deformed sample are refined by the standard sample to eliminate or minimize the effect of the instrumental broadening. Balzar *et al.*^[38] reported a systematic size-strain line broadening analysis of ceria round-robin sample by diffraction measurement with laboratory/synchrotron X-ray sources and constant-wavelength neutron sources. Using the same line broadening analysis method (three comparative analysis), the apparent domain sizes from different diffraction measurements show a good agreement.^[38] Due to the plane stress assumption of the X-ray diffraction technology, the strain values could be away from the neutron diffraction of plain strain assumption. It is reported that the stress variation from neutron diffraction agrees well with X-ray diffraction (layer removal) but with smaller values.^[51,52] Also, it is reported that when combining the three components of the strain, the out-of-plane stresses were found to be smaller at all depths suggesting that the correction for the geometric shifts in the out-of-plane strain is appropriate.^[49] Many functions accepted to analysis of neutron diffraction data are well described and compared in Reference 38. In our paper, one of the most important factors which determines the mechanical behaviors of multiphase materials is the existence of partitioned internal stresses between the constituent components of different phases, which results from their different mechanical responses when the material is stressed.^[53] Gaussian provides a good estimation of the actual strain distribution when analyzing strain broadening of composites by neutron diffraction,^[53] which is also suggested by ISO/TS 21432:2005 international standard method (Non-destructive testing: Standard test method for determining of residual stresses by neutron diffraction) and confirmed in Reference 27.

In order to investigate the deformation behavior of different phases in NAB, dislocations generated around κ phases with various shapes and compositions were observed by TEM, as shown in Figure 10. The larger particle in Figure 10(a) contains 13.6 pct Al, 1.5 pct Cr, 2.1 pct Mn, 59.2 pct Fe, 2.3 pct Ni, and 21.3 pct Cu in atomic percent. The globular dendritic morphology (larger one) and the chemical composition indicate that they are Fe₃Al-based κ_{II} particles. Slip on α matrix was observed near the interface of κ_{II} particle and α phase indicated by the black arrow. After 400 MPa tensile deformation, tangled dislocations around the interface of κ_{IV} and α phase are obvious in Figure 10(b). In addition, twined κ_{IV} particles were also observed which is not found in the lower stressed sample, which could indicate an onset of twin formation after 400 MPa tensile deformation. After 500 MPa tensile deformation, dislocation walls surround a κ_{II} particle indicated in

Figure 10(c). Dislocation density decreases with the increase of the distance away from κ/α interface, shown in Figure 10(d). The dislocations are more severely tangled in contiguous area, and the κ/α interface even becomes obscure compared with the interface shown in Figure 10(a). Two shapes of κ_{III} particles are displayed in Figures 10(e) and (f) after 600 MPa tensile deformation. The round particle in Figure 10(e) contains 28.9 pct Al, 1.4 pct Cr, 1.9 pct Mn, 19.7 pct Fe, 26.0 pct Ni, and 22.1 pct Cu in atomic percent. The near 1:1 ratio of Ni:Al indicates that the round particle is NiAl-based κ_{III} phase. The light strip-shaped particles in Figure 10(e) contain 36.9 pct Al, 1.2 pct Cr, 1.6 pct Mn, 12.1 pct Fe, 31.4 pct Ni, and 16.8 pct Cu in atomic percent, which also reveals an NiAl-based structure. The severely tangled dislocations in α matrix adjacent to κ/α interface are pronounced as pointed by the white arrows. The piled-up dislocations observed in Figure 10 support the explanation in Figure 9 that dislocations pile up at the interfaces of hard κ phases, raise the stress concentration, and increase the internal/residual stresses. The internal stress and the presence of dislocation arrays can change the fracture transition mode of the composite.^[23] This type II stress would also change the crack mechanisms by inducing crack bridging, crack deflection, and microcrack, especially in stress corrosion cracking.^[49] As a widely used marine component, NAB would be more likely to be attacked by stress corrosion crack when deformed or stressed in the ocean.

V. CONCLUSION

The investigation on deformation behavior and deformation microstructure by *in situ* neutron diffraction and TEM was concluded as follows:

Peak shifting and broadening were observed and Gaussian fitting was conducted on neutron diffraction peak profiles of α matrix and κ phases at both holding stress conditions and unloaded stress conditions. For holding stress conditions, lattice strains obtained from peak broadening approach provide smaller values and less information for plastic behavior than those obtained from peak shifting method; for unloaded stress conditions, residual lattice strains from peak broadening estimation indicate no yielding behavior, neither tensile nor compressive character of internal stress, but similar absolute values compared with the residual lattice strains from peak shifting method.

Twinning was observed under TEM in the deformed α grains, with a slight peak asymmetry feature of neutron diffraction peak profiles. It is not obvious that the number of twin faults is significantly increased along with tensile stress. The number of stacking faults in α grains increased with increasing the deformation degree of NAB. Dislocation density obtained from peak broadening method provides a lower value than flow stress method after tensile strain exceeded 0.05, and a close value when strain is around 0.1, but much lower value when tensile strain increased.

Inter-phase stress between α matrix and κ phase is generated at the tensile stress from 300 to 450 MPa which

is in the elasto-plastic region for NAB. The inter-phase stress indicates a tensile internal/residual stress in κ phase and a compressive internal/residual stress in α matrix. Dislocation movement is impeded by various κ phases with different compositions and morphologies, and the dislocation density around α/κ interface of phases increases with increasing the inter-phase stress. In addition, the tangled dislocation density is increased with the distance toward κ/α interface. The piled-up dislocations around hard κ phases raise the stress concentration and then increase the internal stresses.

ACKNOWLEDGMENTS

We would like to acknowledge the financial support provided by the National Basic Research Program of China (973 Program) under Grant No. 2014CB046701 and China Postdoctoral Science Foundation under Grant No. 2014M561471.

REFERENCES

- E.A. Culpán and G. Rose: *Br. Corros. J.*, 1979, vol. 14 (3), pp. 160–66.
- G.W. Lorimer, F. Hasan, J. Iqbal, and N. Ridley: *Br. Corros. J.*, 1986, vol. 21 (4), pp. 244–48.
- A. Al-Hashem and W. Riad: *Mater. Charact.*, 2002, vol. 48 (1), pp. 37–41.
- C.H. Tang, F.T. Cheng, and H.C. Man: *Mater. Sci. Eng. A*, 2004, vol. 373 (1), pp. 195–203.
- E.A. Culpán and G. Rose: *J. Mater. Sci.*, 1978, vol. 13 (8), pp. 1647–57.
- A. Jahanafrooz, F. Hasan, G.W. Lorimer, and N. Ridley: *Metall. Trans. A*, 1983, vol. 14A, pp. 1951–56.
- E.A. Feast and I.A. Cook: *Met. Technol.*, 1983, vol. 10 (1), pp. 121–24.
- F. Hasan, J. Iqbal, and N. Ridley: *Mater. Sci. Technol.*, 1985, vol. 1 (4), pp. 312–15.
- M.D. Fuller, S. Swaminathan, A.P. Zhilyaev, and T.R. Mcnelley: *Mater. Sci. Eng. A*, 2007, vol. 463, pp. 128–37.
- J.A. Wharton, R.C. Barik, G. Kear, R.J.K. Wood, K.R. Stokes, and F.C. Walsh: *Corros. Sci.*, 2005, vol. 47 (12), pp. 3336–67.
- E.E. Danaf, S.R. Kalidindi, and R.D. Doherty: *Metall. Mater. Trans. A*, 1999, vol. 30A, pp. 1223–33.
- F. Greulich and L.E. Murr: *Mater. Sci. Eng.*, 1979, vol. 39 (1), pp. 81–93.
- G.T. Gray: *Acta Metall.*, 1988, vol. 36 (7), pp. 1745–54.
- Y. Zhang, N.R. Tao, and K. Lu: *Scripta Mater.*, 2009, vol. 60 (4), pp. 211–13.
- L. Lu, Y.F. Shen, X.H. Chen, L.H. Qian, and K. Lu: *Science*, 2004, vol. 304 (5669), pp. 422–26.
- A.J. Schwartz, M. Kumar, B.L. Adams, and D.P. Field, eds.: *Electron Backscatter Diffraction in Materials Science*, vol. 2, Springer, New York, 2009.
- G.L. Squires: *Introduction to the Theory of Thermal Neutron Scattering*, Cambridge University Press, Cambridge, 2012.
- Y. Tomota, H. Tokuda, Y. Adachi, M. Wakita, N. Minakawa, A. Moriai, and Y. Morii: *Acta Mater.*, 2004, vol. 52 (20), pp. 5737–45.
- J.S. Jeong, W. Woo, K.H. Oh, S.K. Kwon, and Y.M. Koo: *Acta Mater.*, 2012, vol. 60 (5), pp. 2290–99.
- M.A. Weisser, A.D. Evans, S. Van Petegem, S.R. Holdsworth, and H. Van Swygenhoven: *Acta Mater.*, 2011, vol. 59 (11), pp. 4448–57.
- D.V. Wilson and Y.A. Konnan: *Acta Metall.*, 1964, vol. 12 (5), pp. 617–28.
- N.W. Bonner, G.F. Modlen, P.J. Webster, J.H. Root, and T.M. Holden: *Load-Sharing and Interphase Residual Microstresses in a High Carbon Pearlitic Steel*, vol. 2, ICRS-5, Linköping, Sweden, 1997, pp. 1109–14.
- R.I. Todd, M.A.M. Bourke, C.E. Borsa, and R.J. Brook: *Acta Mater.*, 1997, vol. 45 (4), pp. 1791–1800.
- B.H. Rabin and R.N. Wright: *Metall. Trans. A*, 1992, vol. 23A, pp. 35–40.
- R.G. Baligidad, A. Radhakrishna, and U. Prakash: *Mater. Sci. Eng. A*, 1998, vol. 257, pp. 235–39.
- R.D. Noebe, R.R. Bowman, and M.V. Nathal: *Int. Mater. Rev.*, 1993, vol. 38 (4), pp. 193–232.
- J. Li, H. Wang, G. Sun, B. Chen, Y. Chen, B. Pang, and Y. Zhang: *Nucl. Instrum. Methods Phys. Res. Sect. A*, 2015, vol. 783, pp. 76–79.
- J.W.L. Pang, T.M. Holden, J.S. Wright, and T.E. Mason: *Acta Mater.*, 2000, vol. 48 (5), pp. 1131–40.
- W.M. Tang, Z.X. Zheng, H.J. Tang, R. Ren, and Y.C. Wu: *Intermetallics*, 2007, vol. 15 (8), pp. 1020–26.
- L. Sheng, W. Zhang, J. Guo, F. Yang, Y. Liang, and H. Ye: *Intermetallics*, 2010, vol. 18 (4), pp. 740–44.
- R. Tian and Z. Wang: *Copper Alloys and Processing Manual*, Central South University Press, Changsha, 2002.
- D.E. Armstrong, A.J. Wilkinson, and S.G. Roberts: *J. Mater. Res.*, 2009, vol. 24 (11), pp. 3268–76.
- Y.S. Kim and Y.H. Kim: *Mater. Sci. Eng. A*, 1998, vol. 258, pp. 319–24.
- J.J. Vlassak and W.D. Nix: *J. Mech. Phys. Solids*, 1994, vol. 42 (8), pp. 1223–45.
- K.I. Numakura: *J. Phys. Soc. Jpn.*, 1961, vol. 16, pp. 2344–45.
- P. Lazar and R. Podloucky: *Phys. Rev. B*, 2006, vol. 73 (10), pp. 104–14.
- B. Clausen, T. Lorentzen, and T. Leffers: *Acta Mater.*, 1998, vol. 46 (9), pp. 3087–98.
- D. Balzar, N. Audebrand, M.R. Daymond, A. Fitch, A. Hewat, J.I. Langford, and A. Le Bail: *J. Appl. Crystallogr.*, 2004, vol. 37 (6), pp. 911–24.
- L. Lu, X. Chen, X. Huang, and K. Lu: *Science*, 2009, vol. 323 (5914), pp. 607–10.
- B.E. Warren: *X-ray Diffraction*, 2nd ed., Dover Publications, Mineola, 1990.
- P. Scardi and M. Leoni: *J. Appl. Crystallogr.*, 1999, vol. 32 (4), pp. 671–82.
- F. Hasan, A. Jahanafrooz, G.W. Lorimer, and N. Ridley: *Metall. Trans. A*, 1982, vol. 13A, pp. 1337–45.
- L. Xie, C. Jiang, W. Lu, Q. Feng, and X. Wu: *Surf. Coat. Technol.*, 2011, vol. 206 (2), pp. 511–16.
- G.K. Williamson and R.E. Smallman: *Philos. Mag.*, 1956, vol. 1 (1), pp. 34–46.
- D. Breuer, P. Klimanek, and W. Pantleon: *J. Appl. Crystallogr.*, 2000, vol. 33 (5), pp. 1284–94.
- M.J. Hordon and B.L. Averbach: *Acta Metall.*, 1961, vol. 9 (3), pp. 237–46.
- E.C. Oliver, M.R. Daymond, and P.J. Withers: *Acta Mater.*, 2004, vol. 52 (7), pp. 1937–51.
- B. Clausen, T. Leffers, and T. Lorentzen: *Acta Mater.*, 2003, vol. 51 (20), pp. 6181–88.
- M.T. Hutchings, P.J. Withers, T.M. Holden, and T. Lorentzen: *Introduction to the Characterization of Residual Stress by Neutron Diffraction*, CRC Press, Boca Raton, 2005.
- X. Feaugas: *Acta Mater.*, 1999, vol. 47 (13), pp. 3617–32.
- M.J. Balart, A. Bouzina, L. Edwards, and M.E. Fitzpatrick: *Mater. Sci. Eng. A*, 2004, vol. 367 (1), pp. 132–42.
- D.Q. Wang, I.B. Harris, P.J. Withers, and L. Edwards: in *Proceedings of the 4th European Conference on Residual Stresses*, Cluny, 1996, pp. 69–77.
- R.I. Todd, C. Borsa, B. Derby, and M.A.M. Bourke: *Nucl. Instrum. Methods Phys. Res. Sect. A*, 1995, vol. 354 (1), pp. 139–44.